Supporting Information

Dual-domain solvent-locked electrolyte enabled durable 4.5 V-class sodium batteries

Jiyu Zhang,[1,#] Guochuan Tang,[1,#] Siyu Ma,[1] Longfei Wen,[1] Yongli Cheng,[1] Jun Luo,[1] Xiaoniu Guo,[1] Chen Huang,[1] Enhui Wang,[1,2] Weihua Chen[1*]

[1] College of Chemistry, Zhengzhou University, Kexue Avenue 100, Zhengzhou, Henan 450001, China

[2] Yaoshan Laboratory, Pingdingshan, 467000 Henan, China

[#] These authors contributed equally to this work.

[*] Corresponding authors (e-mails: chenweih@zzu.edu.cn)

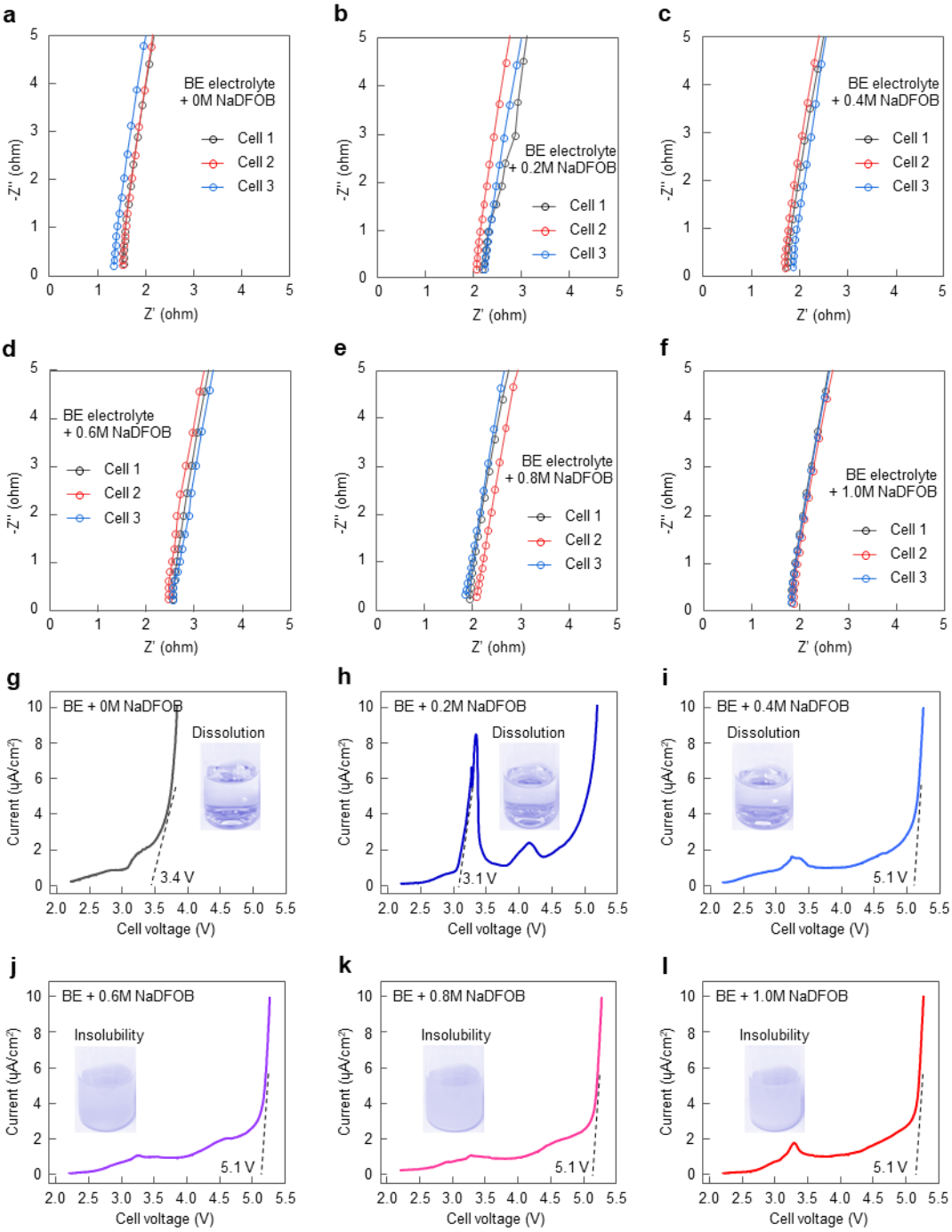

Supplementary Fig. 1 | Physical properties of the baseline electrolytes containing different NaDFOB concentration. EIS plots of symmetric steel sheet||steel sheet cells: (a) 0 M. (b) 0.2 M. (c) 0.4 M. (d) 0.6 M. (e) 0.8 M. (f) 1.0 M. LSV plots of Na||steel sheet cells: (g) 0 M. (h) 0.2 M. (i) 0.4 M. (j) 0.6 M. (k) 0.8 M. (l) 1.0 M.

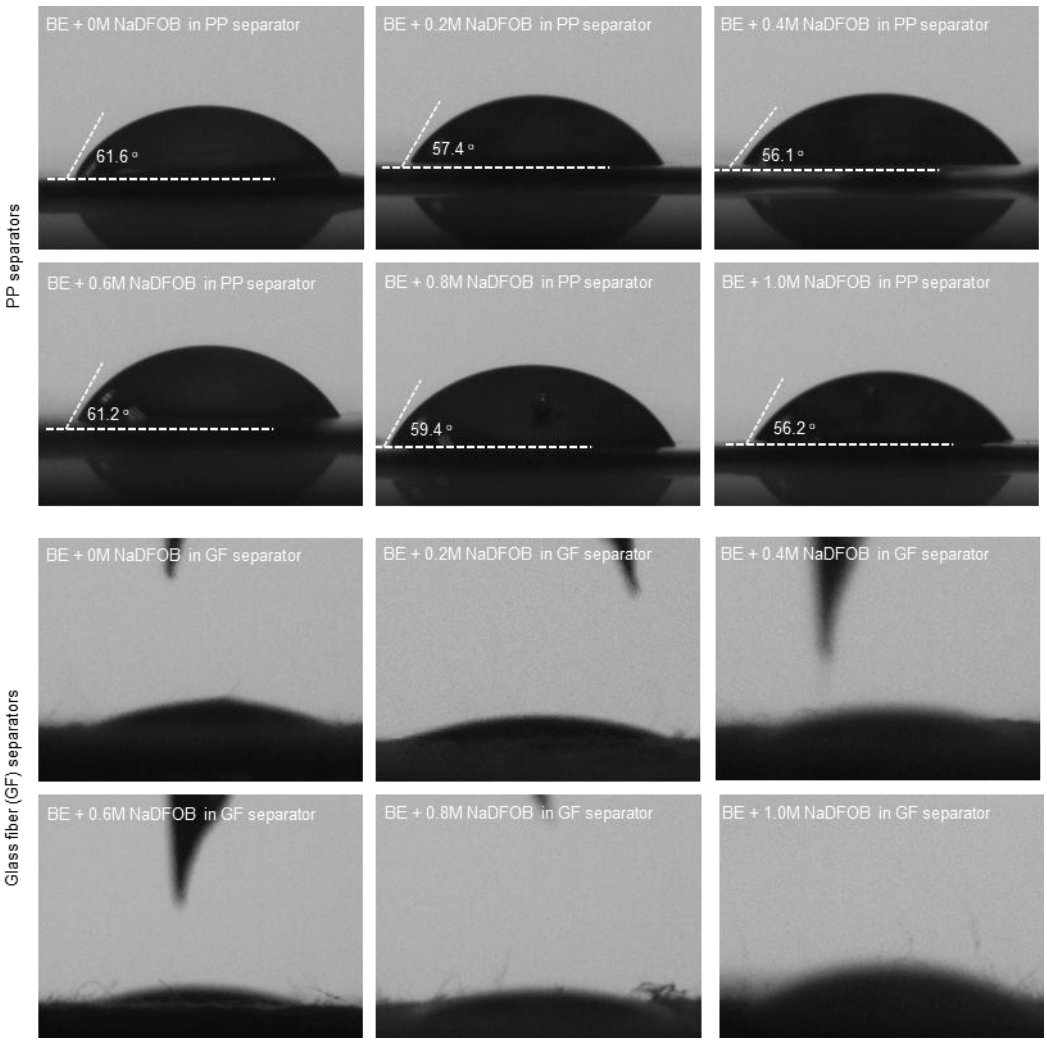

Supplementary Fig. 2 | Contact angle test images of different electrolytes on PP and glass fiber separators. The contact angles of BE electrolytes with 0-1.0 M NaDFOB (at 0.2 M increments) were experimentally determined on PP and glass fiber separators.

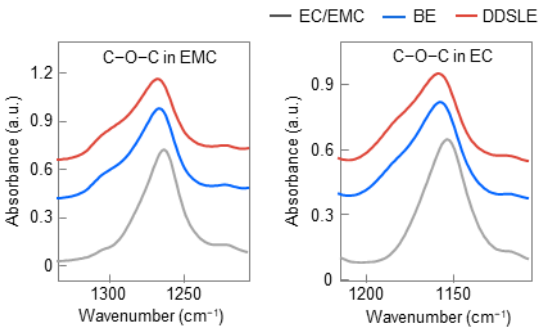

Supplementary Fig. 3 | FTIR spectra tracking salt dissolution in EC/EMC from the BE to the DDSLE electrolytes. In this experiment, the infrared spectrum of the pure solvent (EC/EMC) was measured first. Subsequently, 1M $NaPF_6$ salt was added to obtain the BE electrolyte, followed by the further addition of 0.4M NaDFOB salt to obtain the DDSLE electrolyte. Both spectral scanning and salt addition were performed at intervals of 60 minutes.

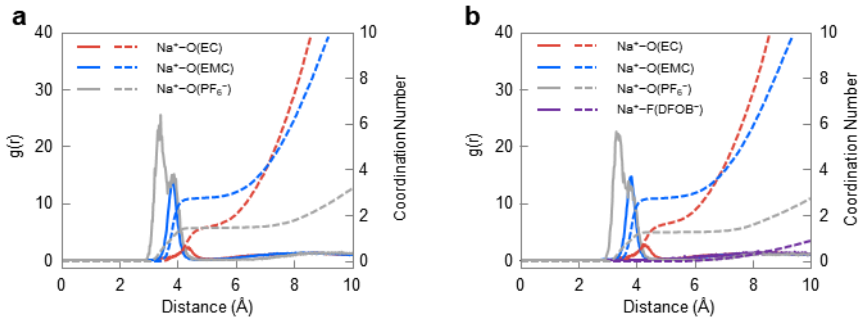

Supplementary Fig. 4 | Radial distribution functions and coordination numbers. (a) BE electrolyte (1M $NaPF_6$ EC/EMC). (b) DDSLE electrolyte (1M $NaPF_6$ EC/EMC + 0.4M NaDFOB).

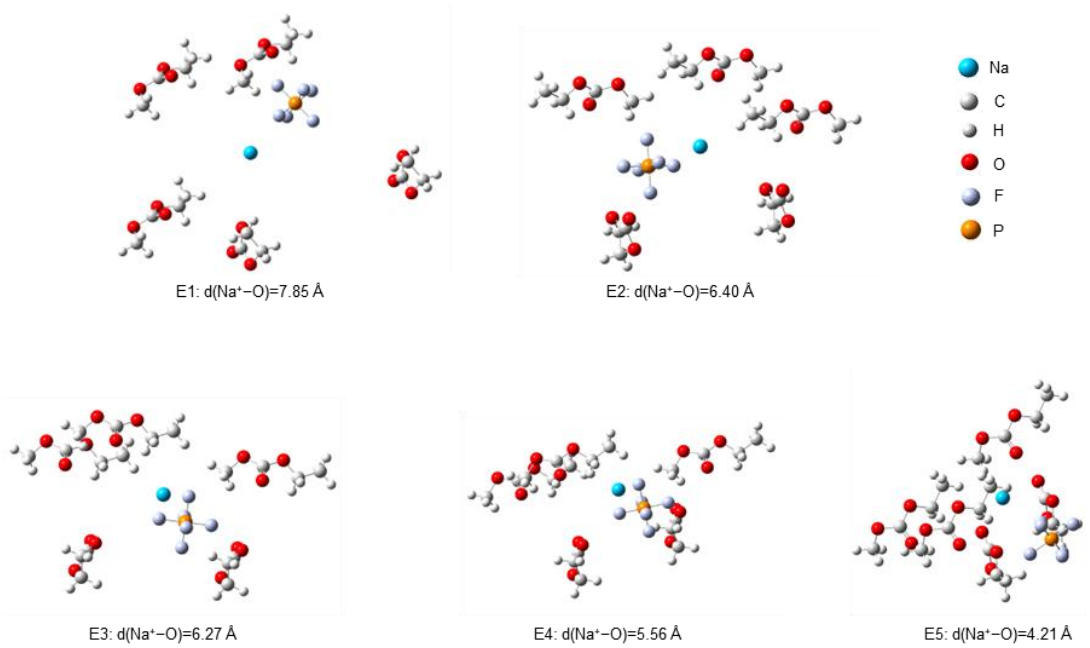

Supplementary Fig. 5 | Na^+ solvation structures with different coordination distances. The coordination distance is the distance between Na^+ and the nearest solvent O atom, where the anion is based on the distance between Na^+ and the nearest F atom.

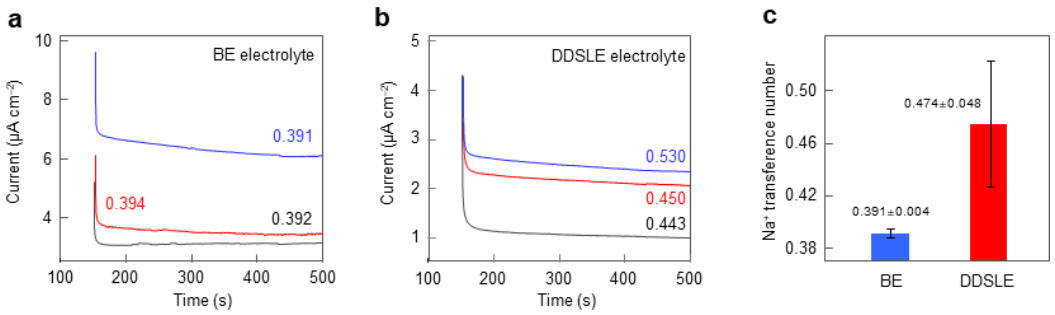

Supplementary Fig. 6 | Chronoamperometry profiles in three Na||Na symmetric cells. (a) BE electrolyte. (b) DDSLE electrolyte. (c) Calculated Na^+ transference number with error bar. The error bar represents the standard deviation of the fitted curve, with data derived from three parallel experiments.

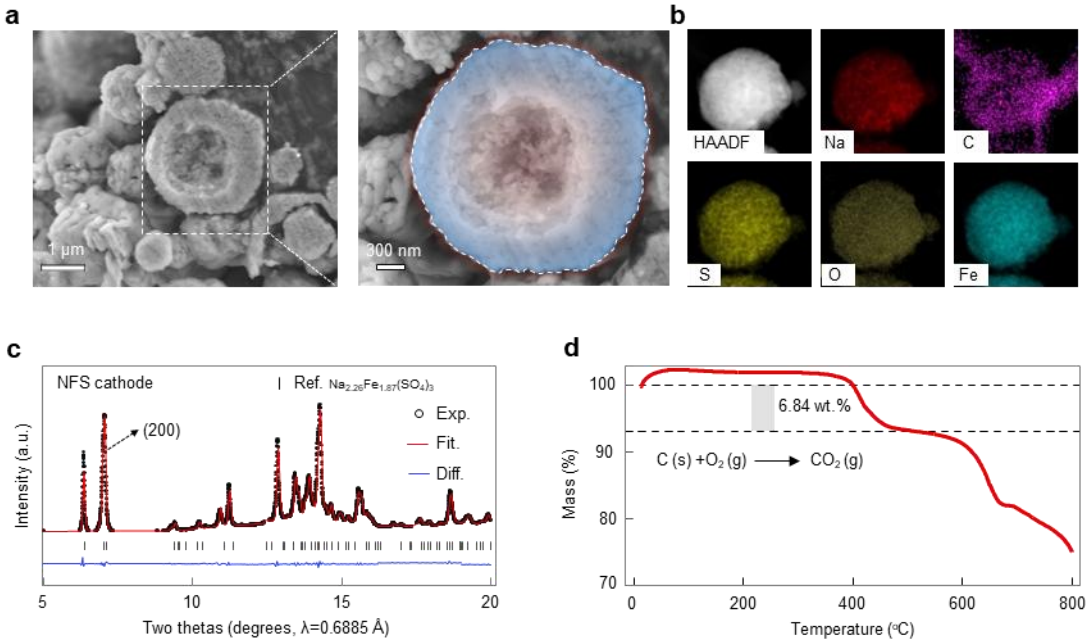

Supplementary Fig. 7 | Structure characteristics of NFS positive electrode material. (a) SEM image. (b) Element mapping images. (c) X-ray diffraction Rietveld refinements. (d) Thermogravimetry curve.

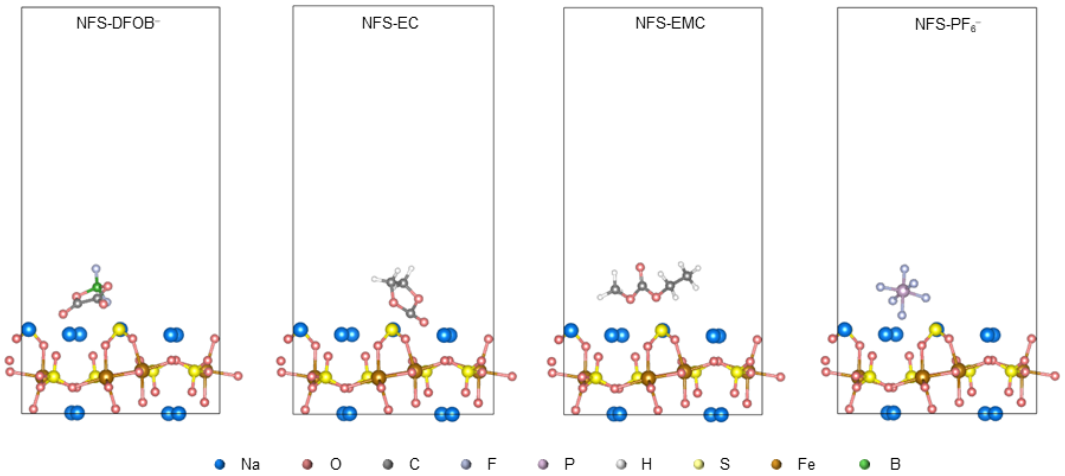

Supplementary Fig. 8 | The adsorption structure model of electrolyte component molecules on NFS (200) surface. The adsorption of EC, EMC, PF_6^-, and $DFOB^-$ in electrolytes on NFS (200) surface was simulated through DFT calculations.

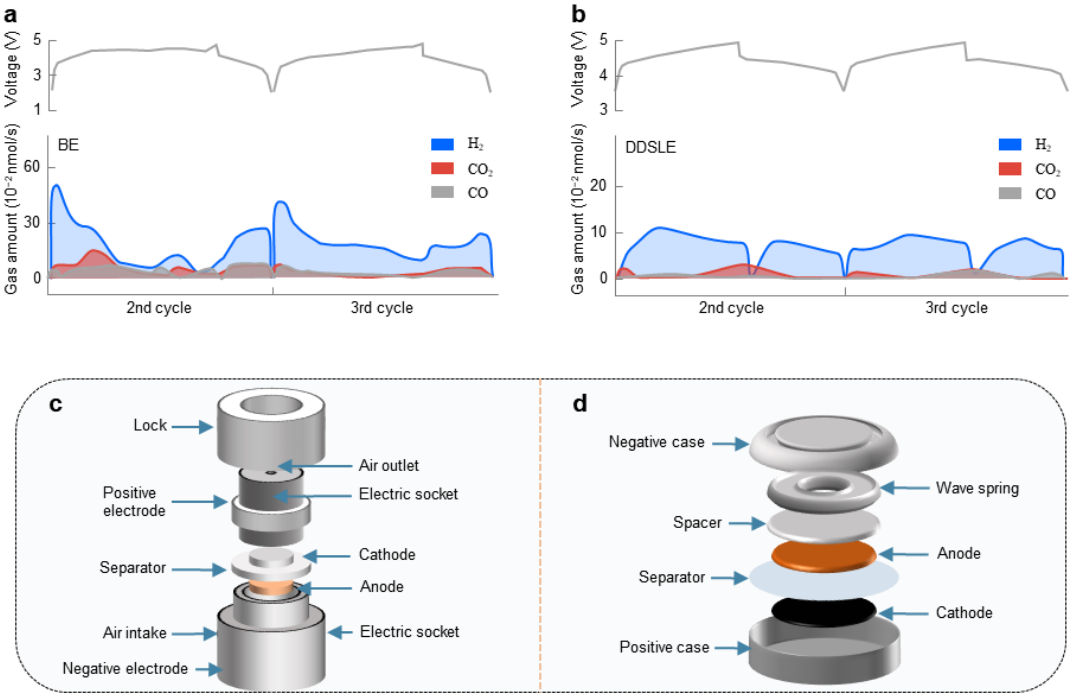

Supplementary Fig. 9 | *In situ* DEMS data for Na||NFS cells during the 2nd and 3rd charge-discharge process to 4.5 V at 50 μA/cm^2 and 25 °C. (a) BE electrolyte. (b) DDSLE electrolyte. Schematic configuration illustrations for (c) custom cell for in situ DEMS cell, (d) Standard coin cell.

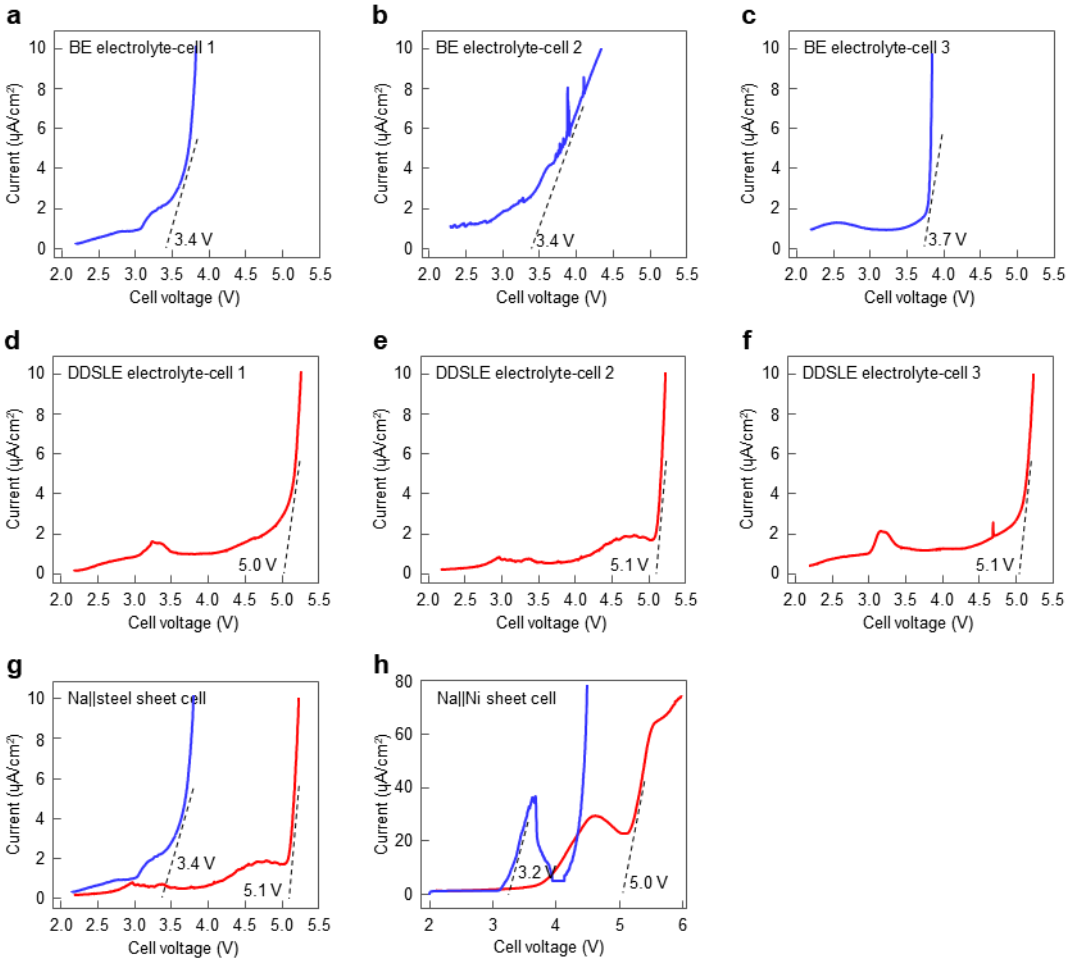

Supplementary Fig. 10 | LSV curves. (a–c) Na||steel sheet cells with BE electrolyte. (d–f) Na||steel sheet cells with DDSLE electrolyte. (g) Na||steel sheet cells with two electrolytes. (h) Na||Ni sheet cells with two electrolytes.

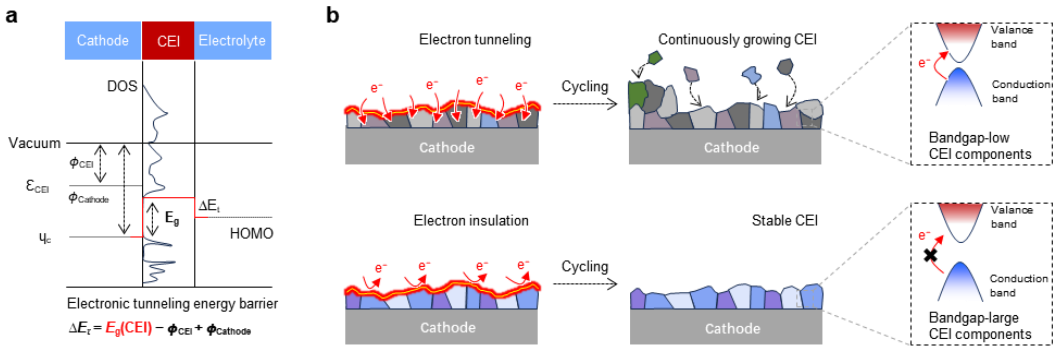

Supplementary Fig. 11 | Schematic illustration of the CEI as an electronic passivation layer. (a) Structure and band alignment of the CEI. (b) Electron tunneling behavior across the CEI.

The CEI acts as an electron-passivating layer between the positive electrode and the electrolyte, with its bandgap E_g(CEI) fundamentally defining the electronic barrier properties. Electron tunneling through the CEI follows quantum mechanical principles, where the transmission probability decays exponentially with both the height and the width of the potential barrier. The bandgap directly governs the barrier height: a larger E_g corresponds to a higher energy barrier, which strongly suppresses electron tunneling, while a smaller E_g reduces the barrier and promotes tunneling. Additionally, the bandgap affects the availability of electronic states within the CEI that can participate in tunneling. Wide-bandgap materials provide fewer accessible states in the relevant energy range, further limiting tunneling probability, whereas narrower bandgaps increase state availability and facilitate electron transfer via direct or trap-assisted tunneling.

In battery operation, a CEI with an appropriately large bandgap can effectively block electron leakage from the positive electrode to the electrolyte, thereby mitigating parasitic reduction reactions and enhancing interfacial stability. This electronic passivation is crucial to suppress continuous CEI growth and electrolyte decomposition, ultimately improving cycling performance. For instance, in this study, boride/fluoride components with bandgaps exceeding 6.2 eV are shown to effectively inhibit electron tunneling above 4.0 V, thereby reducing current leakage and persistent interfacial side reactions.

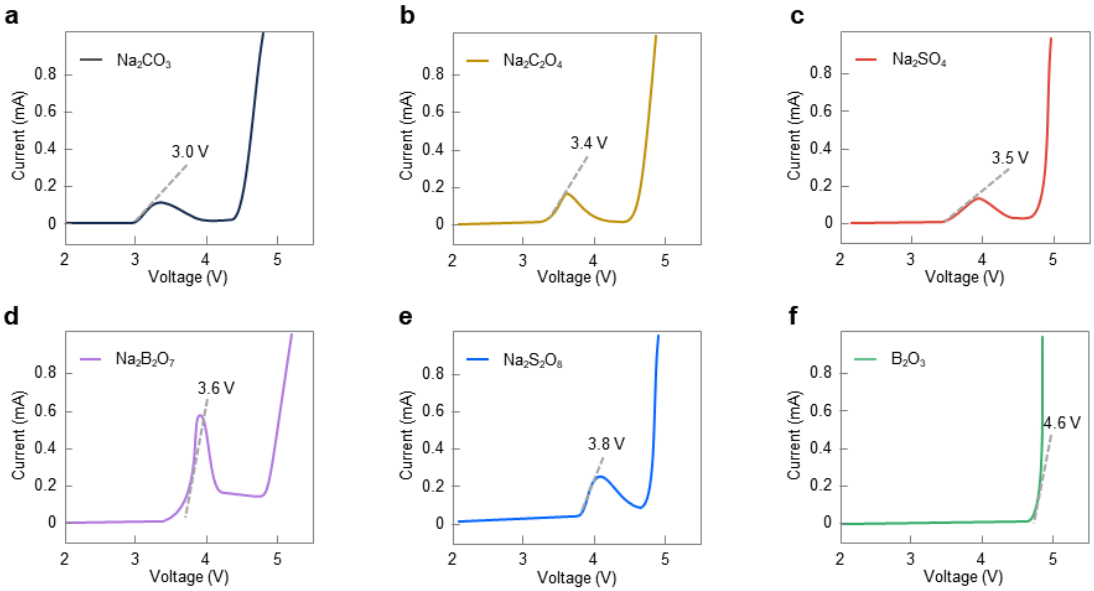

Supplementary Fig. 12 | LSV curves of Na||working electrode. The active materials in working electrodes are: (a) Na_2CO_3. (b) $Na_2C_2O_4$. (c) Na_2SO_4. (d) $Na_2B_2O_7$. (e) $Na_2S_2O_8$. (f) B_2O_3, respectively. The composition of the working electrode is a mixture of active material and PVDF, with a mass ratio of 9:1.

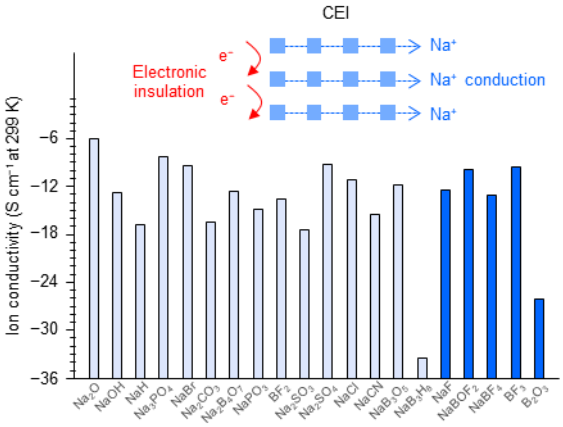

Supplementary Fig. 13 | Calculated Na^+ conductivity of typical CEI inorganics components. These substances are all selected from the Na-based CEI components reported in the literature.

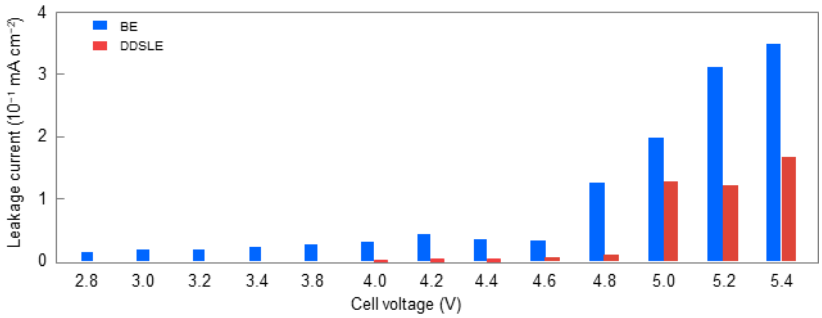

Supplementary Fig. 14 | Leakage current of Na||NFS cells with DDSLE and BE electrolytes during charging to high voltages (>4.5 V). The leakage current value is the average current during the static period after charging to the set voltage.

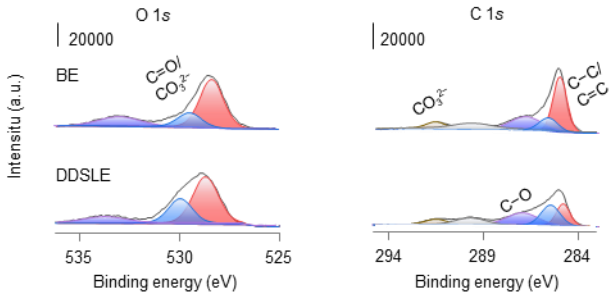

Supplementary Fig. 15 | O 1*s* and C 1*s* XPS spectra of cycled NFS positive electrodes with DDSLE and BE electrolytes, respectively. The electrodes were tested in Na||NFS coin cells at 10 mA g^{-1}, and the battery was cycled for 3 weeks before disassembly and stopped at 2.0V.

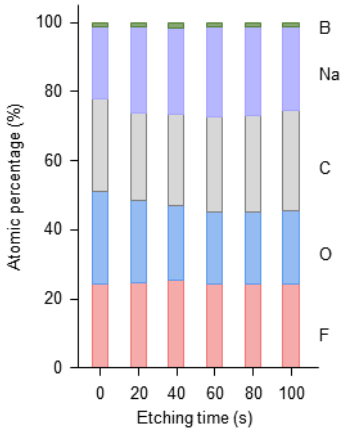

Supplementary Fig. 16 | Etching-dependent element content evolution of cycled NFS positive electrode using DDSLE electrolyte, obtained from XPS survey spectrum. The electrodes were tested in Na||NFS coin cells at 10 mA g^{-1}, and the battery was cycled for 3 weeks before disassembly and stopped at 2.0V.

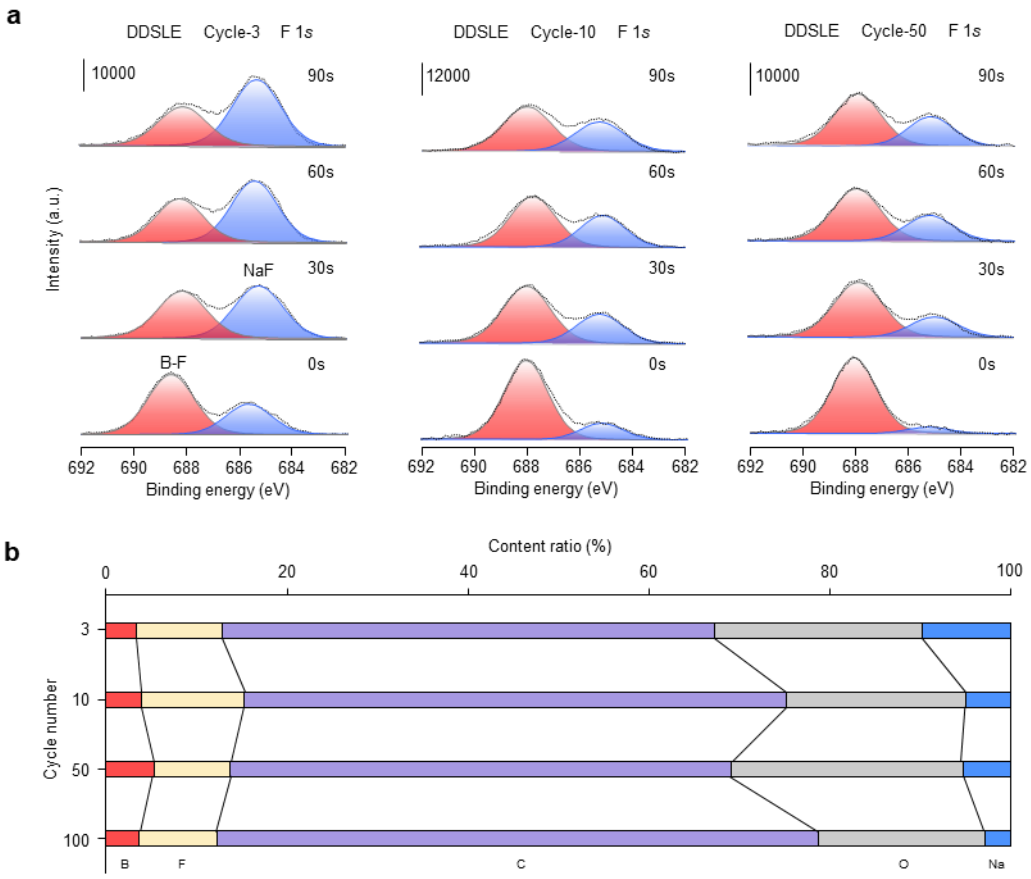

Supplementary Fig. 17 | XPS spectra of cycled NFS positive electrodes after selected cycles using DDSLE electrolyte. (a) F 1*s* spectra. (b) Cycle-dependent element content evolution. The electrodes were tested in Na||NFS coin cells at 10 mA g^{-1}, and the battery was cycled for 3 weeks before disassembly and stopped at 2.0V.

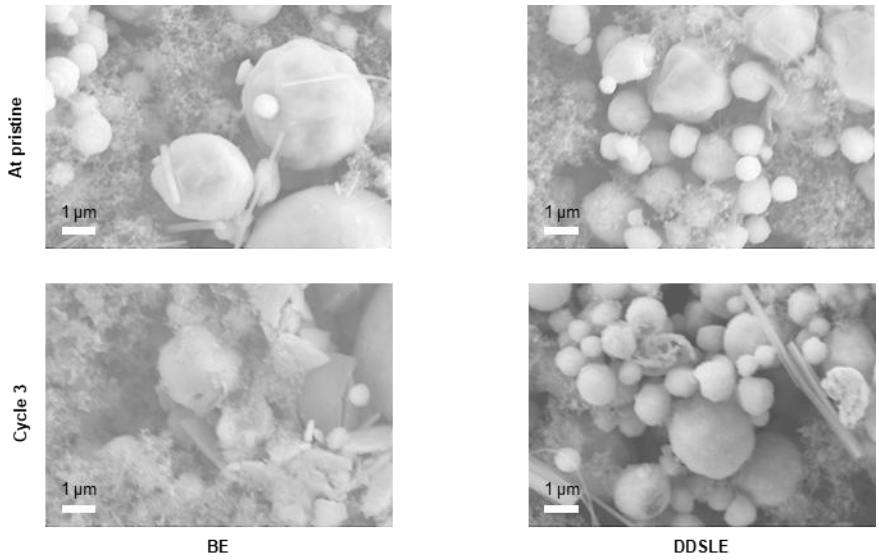

Supplementary Fig. 18 | SEM images of NFS positive electrode at pristine and after 3 cycles at 10 mA g^{-1} and 25 °C. The electrodes were tested in Na||NFS coin cells at 10 mA g^{-1}, and the battery was cycled for 3 weeks before disassembly and stopped at 2.0V.

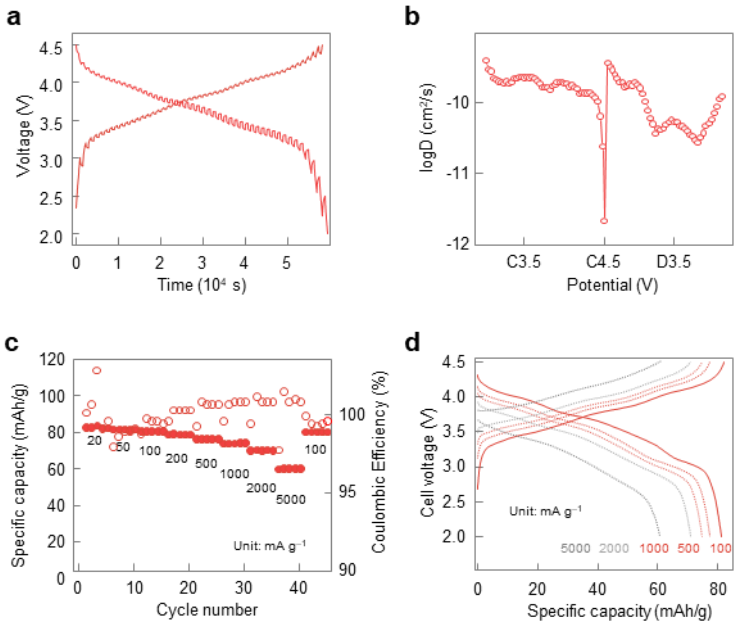

Supplementary Fig. 19 | Reaction kinetics study of DDSLE electrolyte in Na||NFS coin cells. (a) GITT curves. (b) Calculated Na^+ conductivity. (c) Rate performance. (d) Galvanostatic charge–discharge profiles.

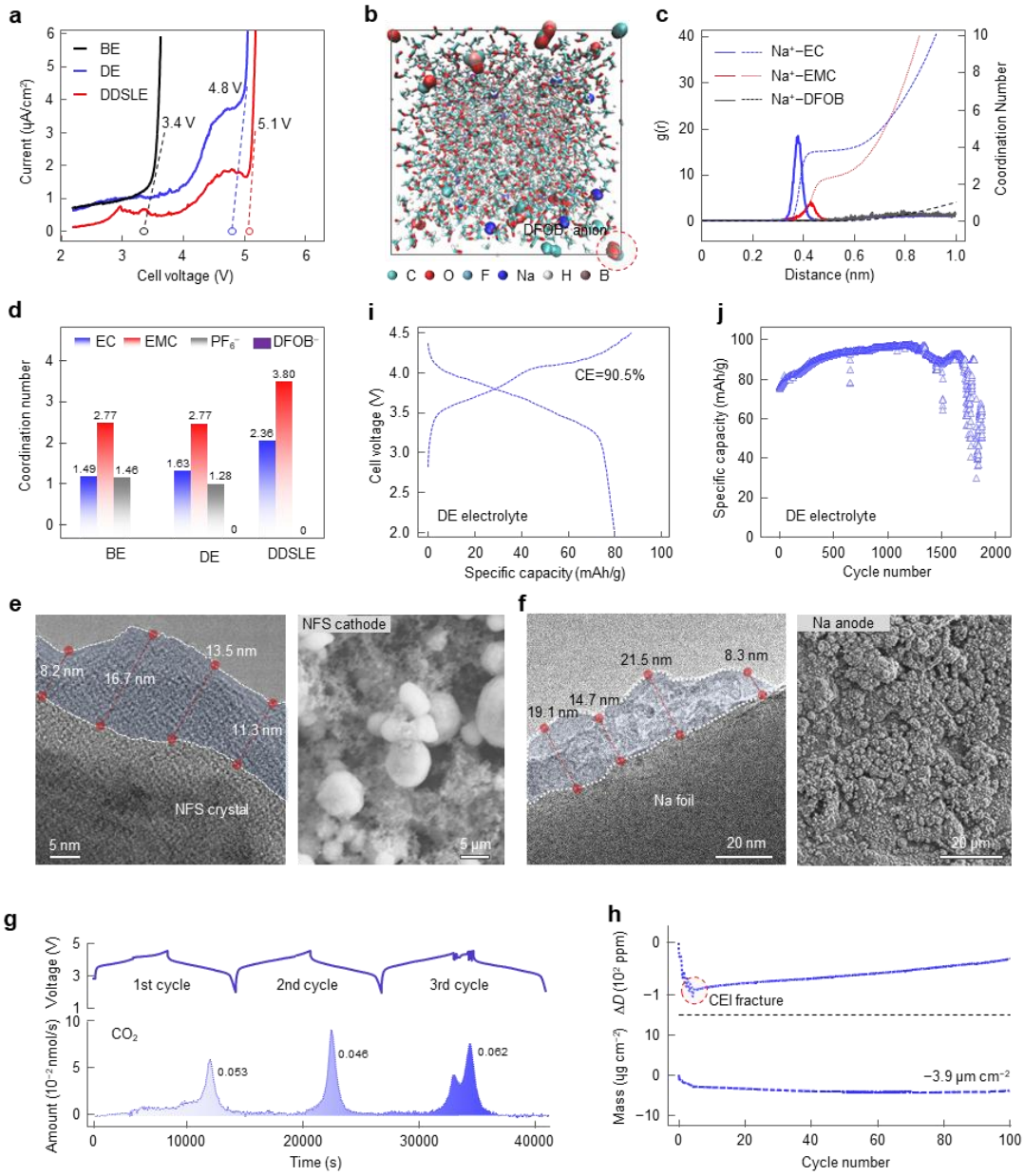

Supplementary Fig. 20 | Solvation configuration, interphase structure, and battery performance of DE electrolyte. (a) LSV curves. (b) Snapshots from MD simulations. (c) Radial distribution functions and coordination numbers. (d) Average coordination numbers obtained from MD simulations. TEM and SEM images of (e) NFS positive electrode and (f) Na negative electrode after 3 cycles at 10 mA g^{-1} and 25 ºC. (g) *In situ* DEMS data for Na||NFS cell at 50 μA and 25 ºC. (h) Time-dependent changes in mass (Δm) and energy dissipation (ΔD) for a Na||NFS cell over multiple cycles during CV measurement at 50mV/s and 25 ºC recorded via *in situ* EQCM. (i) Galvanostatic charge–discharge profiles at 1st cycle at 10 mA g^{-1} and 25 ºC, (j) cycling performance of Na||NFS coin cells using DE electrolyte at 100 mA g^{-1} and 25 ºC. The electrodes in Figures e and f were tested in Na||NFS coin cells at 10 mA g^{-1}, and the battery was cycled for 3 weeks before disassembly and stopped at 2.0V.

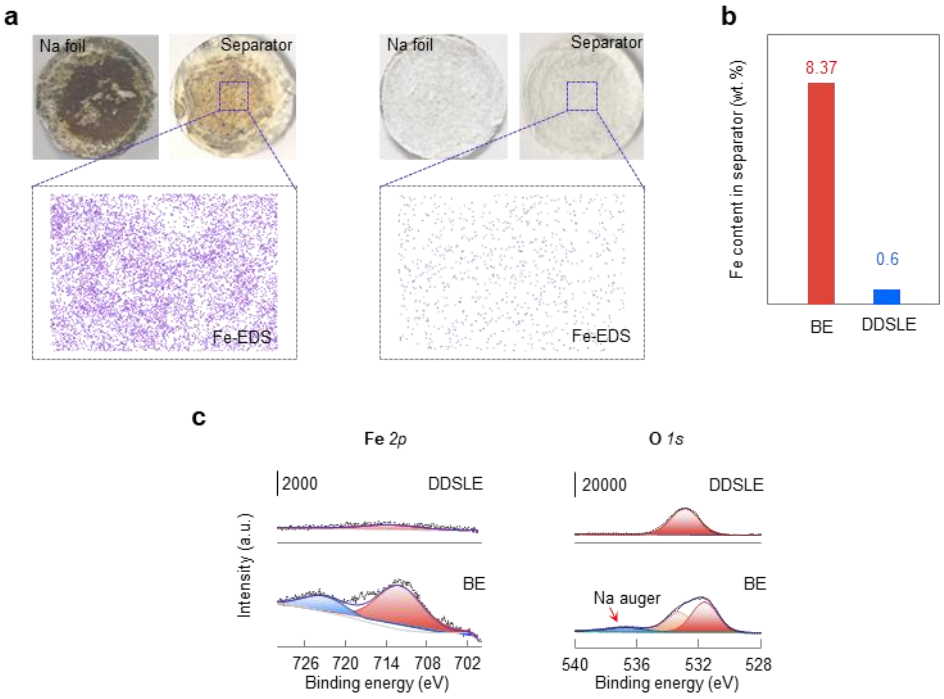

Supplementary Fig. 21 | Post-mortem analysis from disassembled 500-cycled Na||NFS coin cells at 1000 mA g^{-1} and 25 °C. (a) Digital photos of the diaphragm and EDS Fe element scanning images. (b) Fe element contents. (c) XPS spectra of cycled separators. The electrode was tested in Na||NFS button cell at 1000 mA g^{-1}, and the cell was cycled for 500 cycles before disassembly and stopped at 2.0V.

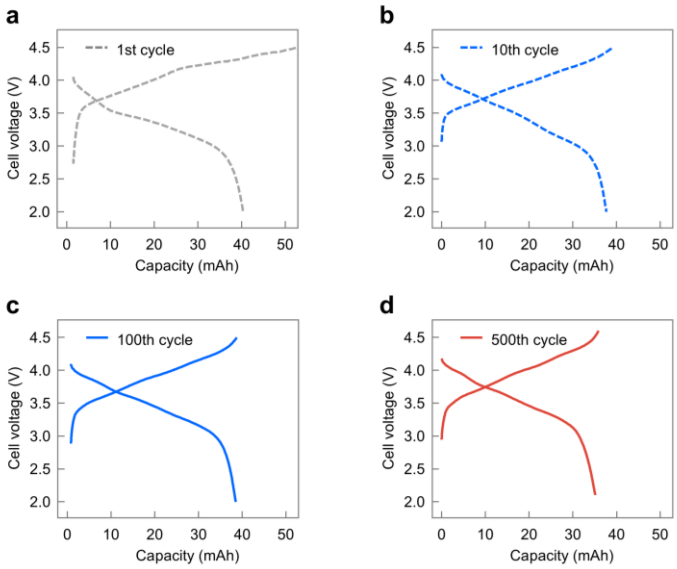

Supplementary Fig. 22 | Galvanostatic charge–discharge profiles of Na||NFS pouch cells at selected cycles (testing conditions: 100 mA g^{-1} and 25 °C). (a) 1st. (b) 10th. (c) 100th. (d) 500th.

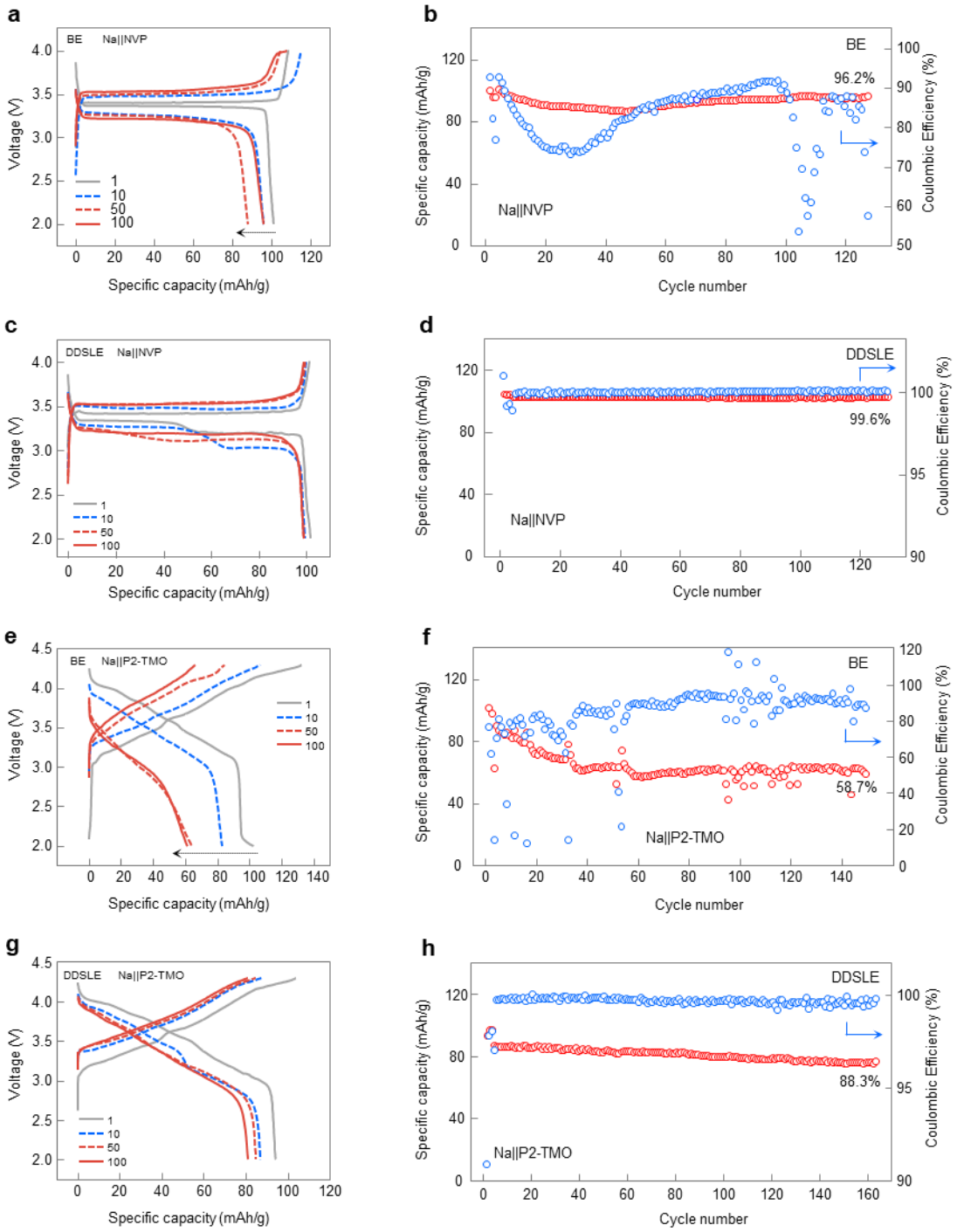

Supplementary Fig. 23 | Electrochemical performance of DDSLE electrolyte in Na-metal coin cells using different positive electrodes. Galvanostatic charge–discharge profiles of (a, c) Na||NVP, and (e, g) Na||P2-TMO coin cells at 100 mA g^{-1} and 25 °C. Cycling performance of (b, d) Na||NVP, and (f, h) Na||P2-TMO coin cells at 100 mA g^{-1} and 25 °C. (a, b, e, f) BE electrolyte. (c, d, g, h) DDSLE electrolyte.

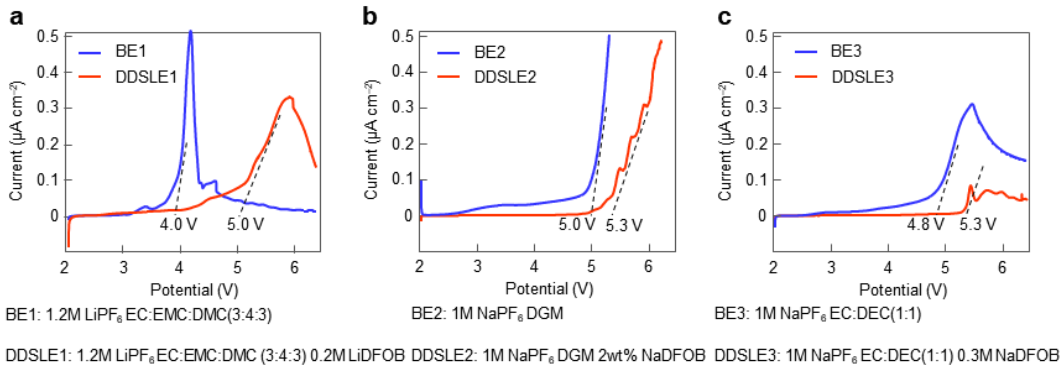

Supplementary Fig. 24 | LSV curves in metal||steel sheet cells. (a) Li||steel sheet cells with BE1 and DDSLE1 electrolytes. (b) Na||steel sheet cells with BE2 and DDSLE2 electrolytes. (c) Na||steel sheet cells with BE3 and DDSLE3 electrolytes.

Supplementary table 1 | Detailed XRD diffraction refinement results of $Na_{2+2x}Fe_{2-x}(SO_4)_3$ (monoclinic, C2/c).

Atom	x	y	z	frac	Crystal
Na1	0.5000	0.7266	0.7500	1.0	
Na2	0.0000	0.0000	0.0000	0.7130	
Na3	0.5000	0.9570	0.2500	0.5432	
Fe	0.7323	0.1572	0.1362	0.9359	$Na_{2.26}Fe_{1.87}(SO_4)_3$
S1	0.0000	0.7821	0.7500	1.0	Space group: C2/c,
S2	0.7469	0.5909	0.8710	1.0	*a*=12.65 Å,
O1	0.0970	0.8310	0.7030	1.0	*b*=12.77 Å,
O2	0.4560	0.2090	0.5530	1.0	*c*=6.52 Å,
O3	0.7471	0.6510	0.6770	1.0	*V*=948.85 Å^3
O4	0.3545	1.0014	0.376	1.0	
O5	0.4020	0.5708	0.6760	1.0	
O6	0.3170	0.1468	0.0370	1.0	

Supplementary table 2 | Detailed material parameters, ID number for BVS calculations.

Materials	Material ID	Bandgap (eV)	Na^+ conductivity (mS/cm)
B_2O_3	mp-717	8.38	9.12E-27
BF_3	mp-558149	8.14	2.80E-10
$NaBF_4$	mp-3521	7.85	9.41E-14
$NaBOF_2$	mp-1194338	6.3	1.43E-10
NaF	mp-682	6.2	3.02E-13
NaB_3H_8	mp-1190348	5.78	3.43E-34
NaB_3O_5	mp-557406	5.44	1.37E-12
NaCN	mp-30053	5.04	2.95E-16
NaCl	mp-22862	5	6.68E-12
Na_2SO_4	mp-4770	4.99	4.66E-10
Na_2SO_3	mp-21282	4.92	3.29E-18
BF_2	mp-27864	4.9	2.87E-14
$NaPO_3$	mp-648053	4.84	1.32E-15
$Na_2B_4O_7$	mp-17941	4.77	2.75E-13
Na_2CO_3	mp-1201027	4.19	2.94E-17
NaBr	mp-22916	4.09	3.14E-10
Na_3PO_4	mp-674333	3.92	5.66E-09
NaH	mp-23870	3.77	1.34E-17
NaOH	mp-23940	2.82	1.71E-13
Na_2O	mp-2352	1.87	9.68E-07

Supplementary table 3 | Comparison of Na||NFS cells based on DDSEL electrolyte with other reported SIBs.

Positive electrode	Negative electrode	Electrolyte	Decay rate per cycle	Cycle number /rate	Cut-off voltage	Positive electrode material/thickness	Electrolyte	Temperature	Negative electrode thickness	Ref.
$Na_{2.26}Fe_{1.87}(SO_4)_3$	**Na**	**1M $NaPF_6$ + 0.4M NaDFOB in EC/EMC**	**$7.15*10^{-4}$**	**16500/5C**	**4.5 V**	**1.8-2.6 mg cm^{-2} /33-49 μm**	**120 μL**	**25 ± 1 °C**	**70 μm s**	**This work**
$Na_{2.4}Fe_{1.8}(SO_4)_3$	Na	1M $NaClO_4$ in EC/DEC	0.0042	10000/10C	4.5 V	/	/	room temperature	/	*J. Energy Chem.* **2021**, 54, 564
$Na_{2.4}Fe_{1.8}(SO_4)_3$	$NaTi_2(PO_4)_3$	1M $NaClO_4$ in EC/PC + 5% FEC	0.00293	10000/10C	4.5 V	8 -9.5 mg cm^{-2}	/	25℃	/	*Adv. Funct. Mater.* **2024**, 35, 2411007
$Na_{6-2x}Fe_x(SO_4)_3$	Na	1M $NaClO_4$ in EC/DEC + 5% FEC	0.00276	10000/30C	4.5 V	/	/	2–2.5℃	/	*Science Bulletin* **2023**, 68, 1894
$Na_{2.5}Fe_2(SO_4)_{2.5}(PO_4)_{0.5}$	Na	1M $NaClO_4$ in EC/DEC + 5% FEC	0.00112	10000/10C	4.5 V	1.5 mg cm^{-2}	/	/	/	*J. Am. Chem. Soc.* **2025**, 147, 14635−14646
$Na_{2.9}Fe_{1.7}(SO_4)_{2.7}(PO_4)_{0.3}$	Na	1M $NaClO_4$ in EC/DEC + 5% FEC	0.00395	6000/30C	4.5 V	1.5 - 2.0 mg cm^{-2}	/	/	/	*Nano Energy* **2024**, 125, 109557
$Na_2Fe(SO_4)_2$	Na	1M $NaPF_6$ in EC: DMC	0.00231	3500/3C	4.5 V	/	/	/	/	*Energy Storage Mater.* **2025**, 74, 103882
$Na_{2.26}Fe_{1.87}(SO_4)_3$	Na	1M $NaClO_4$ in EC/PC + 5% FEC	0.00608	5700/5C	4.5 V	1.5–2.0 mg cm^{-2}	120 uL	/	/	*Nat. Commun.* **2023**, 14, 3701
$Na_{2.466}Fe_{1.724}Mg_{0.043}(SO_4)_3$	Na	1M $NaClO_4$ in EC/PC + 5% FEC	0.00584	5000/5C	4.5 V	1–1.5 mg cm^{-2}	120 uL	/	/	*eScience*, **2025**, 5, 100313
$Na_6Fe_5(SO_4)_8$	Na	1M $NaClO_4$ in PC	0.001	1000/2C	4.5 V	2 mg cm^{-2}	/	/	/	*J. Mater. Chem. A* **2019**, 7, 14656
$Na_4Fe_3(PO_4)_2(P_2O_7)$	Na	1M $NaClO_4$ in PC + 5% FEC	0.0014	5000/20C	4.1 V	/	/	/	/	*Angew. Chem. Int. Ed.* **2025**, 64, e20250269
$Na_4Fe_3(PO_4)_2(P_2O_7)$	Na	1M $NaClO_4$ in EC/PC + 5% FEC	0.00286	10000/50C	4.3 V	1.2-1.4 mg cm^{-2}	/	/	/	*J. Am. Chem. Soc.* **2025**, 147, 16, 13905
$Na_3V_2(PO_4)_3$	Na	EC/PC/EP-NaDFOB/SN	0.00204	7000/5C	3.9 V	2.0-3.0 mg cm^{-2}	/	25℃	/	*Angew. Chem. Int. Ed.* **2024**, 63, e202401051
$Na_3V_2(PO_4)_3$	Na	1M $NaPF_6$ in diglyme	0.00345	2000/50C	4.2 V	2.0 mg cm^{-2}	/	/	/	*ACS Nano* **2024**, 18, 9354–9364
$Na_{3.6}VMn_{0.4}Fe_{0.4}Ti_{0.1}Zr_{0.1}(PO_4)_3$	Na	1M $NaClO_4$ in EC/DEC + 5% FEC	0.00194	10000/10C	3.8 V	/	/	/	/	*Adv. Energy Mater.* **2025**, 15, 2500502
$Na_3V_2(PO_4)_3$	Na	0.75M $NaClO_4$ FEC/PC + 0.01M LiTFSI	0.00108	10000/60C	3.8 V	/	/	/	/	*J. Am. Chem. Soc.* **2023**, 145, 21661
$Na_{0.67}Fe_{0.3}Mn_{0.7}O_2$	Na	1M $NaClO_4$ in PC + 5% FEC	0.058	300/2C	4.2 V	2-3 mg cm^{-2}	/	/	/	*Adv. Funct. Mater.* **2025**, 35, 2504354
$Na_{0.44}Mn_{0.85}Ti_{0.15}O_2$	Na	1M $NaClO_4$ in EC/DEC + 5% FEC	0.02231	650/2C	4.0 V	2-3 mg cm^{-2}	/	25℃	/	*Adv. Mater.* **2024**, 36, 2407994
$Na_{0.75}Li_{0.25}Mn_{0.75}O_2$	Na	1M $NaClO_4$ in PC + 5% FEC	0.0876	100/0.2C	4.4 V	2–3 mg cm^{-2}	/	/	/	*Energy Environ. Sci.* **2025**, 18, 7995–8008
$Na_{0.61}Ca_{0.05}[Li_{0.1}Ni_{0.23}Mn_{0.67}]O_{1.95}F_{0.}$	Na	1M $NaClO_4$ in EC/DEC	0.01818	1100/16C	4.3 V	2 mg cm^{-2}	/	/	/	*Adv. Mater.* **2024**, 36, 2407519

$NaNi_{0.3}Cu_{0.1}Fe_{0.2}Mn_{0.3}Ti_{0.1}O_2$	Na	1M $NaClO_4$ in EC/DEC/DMC	0.03	500/1C	4.0 V	/	/	/	/	*Nat. Energy* **2024**, 9, 1529–1539
$Na_{0.8}Cu_{0.22}Li_{0.08}Mn_{0.67}O_2$	Na	1M $NaClO_4$ in PC + 5% FEC	0.036	500/10C	4.4 V	3~4 mg cm^{-2}	/	/	/	*J. Am. Chem. Soc.* **2023**, 145, 22708
O3-$Na_{0.8}Li_{0.2}Fe_{0.2}Ru_{0.6}O_2$	Na	1M $NaClO_4$ in EC/PC + 5% FEC	0.046	100/1C	4.5 V	/	/	/	/	*J. Am. Chem. Soc.* **2024**, 146, 13924
$Na_{2-x}Mn_{0.8}Fe_{e0.2}[Fe(CN)_6]_y \cdot n$	Na	1M $NaClO_4$ in EC/DEC + 5% FEC	0.0406	500/1C	4.0 V	2 mg cm^{-2}	100 μL	25 ºC	/	*ACS Nano* **2025**, 19, 22093
Prussian blue	Na	1M $NaClO_4$ in EC/DEC + 5% FEC	0.00525	4000/20C	4.1 V	/	/	/	/	*Angew. Chem. Int. Ed.* **2025**, 64, e202421916
$Na_{1.34}Ni[Fe(CN)_6]$	Na	1M $NaClO_4$ in EC/DEC + 5% FEC	0.00269	13000/5C	4.2 V	1.5-2 mg cm^{-2}	/	25 ºC	/	*Small* **2025**, 21, 2407570
FeHCF-P	Na	1M $NaClO_4$ in EC/DEC + 5% FEC	0.034	500/1C	4.1 V	1.5 mg cm^{-2}	150 μL	25 ºC	/	*Nano-Micro Lett.* **2022**, 14, 9
$Na_{1.76}FeFe(CN)_6 \cdot 2.6H_2O$	Na	1M $NaClO_4$ in EC/PC + 3% FEC	0.00875	2000/5C	3.8 V	2 mg cm^{-2}	/	/	/	*Adv. Funct. Mater.* **2022**, 32, 2111727
$Na_2Mn_{0.2}Fe_{0.2}Co_{0.2}Ni_{0.2}Cu_{0.2}[Fe(C$	Na	1M $NaClO_4$ in EC/DEC + 5% FEC	0.00393	9000/5C	4.2 V	/	/	/	/	*Angew. Chem. Int. Ed.* **2025**, 64, e20251289

Supplementary table 4 | Comprehensive evaluation on various Na-metal pouch cells.

System	Separator compatibility	Safaty	Operation voltage (V)	Side reactions	Positive electrode material/ thickness	Electrolyte	Tempe rature	Negative electrode thickness	Cycling stability (capacity retention, X cycles at Y mA g^{-1})	Ref.
Na||NFS pouch cell 1M $NaPF_6$ + 0.4M NaDFOB EC/EMC	**Good**	**Good**	**2.0–4.5 V**	**Good**	**7 mg cm^{-2} /89 μm**	**6.22 μL cm^{-2}**	**25 ± 1 °C**	**70μm**	**86%, 500 cycles, 1C**	**This work**
Na||NVP pouch cell 0.8M NaTFSI, EC : TTE : BBE = 4: 2: 1	Fair	Fair	2.3–3.8 V	Good	/	60 μL cm^{-2}	/	100 μm	97.9%, 264 cycles, 1C	*Energy Environ. Sci.*, **2024**, 17, 791–799
Na||NVP pouch cell 0.75M $NaClO_4$ FEC/PC (1/1) 0.01 M LiTFSI	Poor (High viscosity)	Poor (Poor thermal stability)	2.5–3.8 V	Fair (Current collector corrosion)	/	/	/	/	94.2%, 50 cycles, 5C	*J. Am. Chem. Soc.* **2023**, 145, 21661–21671
Na||$NaFe_{1/3}Ni_{1/3}Mn_{1/3}O_2$ pouch cell 3.0 M NaFSI, DME +0.3M isosorbide dinitrate	Good	Poor (Poor thermal stability)	2.0–3.95	Poor (Current collector corrosion)	/	/	/	/	98.03%, 30 cycles, 0.1C	*Adv. Mater.* **2025**, e17094
Na||NFS pouch cell 1M $NaClO_4$ EC/PC+5 wt.% FEC	Poor (High viscosity)	Poor (Explosive)	2.0–4.5 V	Fair	/	/	/	/	0.032%; 87.2%, 400 cycles, 1C	*Adv. Funct. Mater.* **2025**, 2504599

Supplementary note 1

We further evaluated the oxidation stability of electrolytes with varying NaDFOB concentrations, and the results demonstrate a clear trend.

(1) Trend in oxidation stability with NaDFOB concentration

LSV curves reveal a strong dependence of oxidation stability on NaDFOB concentration. The baseline electrolyte (BE, without NaDFOB) begins to decompose at approximately 3.4 V. Upon adding 0.2M NaDFOB, a new oxidation peak emerges between 3.0 and 3.6 V, corresponding to the preferential decomposition of $DFOB^-$ anions. By applying a threshold current density of 6 μA cm^{-2}, the oxidative stability limit is determined to be 3.1 V. When the NaDFOB concentration is increased to 0.4 M, the pre-decomposition peak at 3.0 V is suppressed to below 1.8 μA cm^{-2}, and the oxidative stability limit is significantly raised to 5.1 V. Further increases in NaDFOB concentration are limited by salt solubility, leading to precipitate formation and no further improvement in oxidation limit.

(2) Underlying mechanism

This trend is attributed to the distinct roles of $DFOB^-$ anions within the bulk electrolyte and at the positive electrode interface.

In the baseline electrolyte (BE) without NaDFOB, oxidation decomposition is governed by a loosely coordinated carbonate-based solvation sheath and abundant free solvent molecules, leading to initiation at relatively low voltages.

At a low NaDFOB concentration (0.2M), the limited $DFOB^-$ anions are insufficient to concurrently establish a solvent-reinforced Na^+ solvation structure with bulk solution and anion-rich shield at the positive electrode interface. Consequently, most $DFOB^-$ anions preferentially accumulate and decompose at the positive electrode surface due to their strong binding affinity toward Na^+. However, the resulting insoluble products cannot form an integrated passivation interphase, resulting in partial decomposition of coordinated and free solvent molecules.

When the NaDFOB concentration reaches 0.4M, sufficient $DFOB^-$ anions enables the establishment of a dual-domain solvent-locked effect. This dual-domain solvent-locked effect significantly restricts the degrees of freedom and reactivity of the solvent molecules, thereby raising the oxidation stability limit to 5.1V and inhibiting subsequent decomposition of other electrolyte components.

Supplementary note 2

The apparent conceptual opposition between the "solvent-reinforced solvation structure" proposed here and the widely reported "weak-solvation structures" is well-founded. However, the fact that both strategies significantly enhance electrolyte stability is not a logical paradox. Instead, it stems from their targeted optimization of distinct, dominant failure mechanisms within the electrochemical system. Their core divergence lies in the deliberate design of the solvation structure, yet both ultimately promote stability by enabling effective interfacial protection.

(1) Explanation of the seemingly opposition

(a) Solvent-reinforced strategy

Structural feature: a tight, thermodynamically stable solvation sheath dominated by solvents.

Typical implementation: using high-donor-number solvents or specific coordinating molecules.

Key design principle: strengthening the interaction between solvent and cation.

Stability mechanism: this structure directly improves the intrinsic oxidation resistance of the electrolyte by lowering HOMO energy level of the coordinated solvent-cation unit. Additionally, the "locked" solvent molecules within the sheath reduce side reactions caused by their free movement.

(b) Weakly solvating strategy

Structural feature: a loose solvation sheath rich in contact ion pairs or aggregates, where anions enter the inner coordination sphere.

Typical implementation: employing low-donor-number solvents or high-concentration electrolytes.

Key design principle: weakening solvent-cation binding to promote anion participation in solvation.

Stability mechanism: it shifts the HOMO location of solvation sheath from the solvent towards the salt (*Nat. Energy*, **2019**, 4, 269–280). This induces the preferential decomposition of anions at interfaces, forming a dense, ion-conductive interphases while kinetically suppressing solvent decomposition.

While the core design principles (strengthening *vs.* weakening solvent-cation binding) are indeed opposing, the fundamental distinction lies in actively controlling the coordination competition within the cation's primary solvation shell to dictate interfacial reaction pathways.

(2) Explanation for the enhanced electrolyte stability

The key to understanding this seemingly contradictory phenomenon is recognizing that both strategies achieve the same ultimate goal—constructing a stable electrode/electrolyte interface via fundamentally different pathways. They address the problem from two complementary dimensions: thermodynamics and kinetics.

(a) Solvent-reinforced strategy

It primarily focuses on thermodynamic stability. It creates a more inert bulk electrolyte by reducing the reactivity of its components. Its robust solvation sheath undergoes a controlled, orderly decomposition at interfaces, tending to yield stable products.

(b) Weakly solvating strategy

It primarily excels at kinetic optimization. By lowering the desolvation energy barrier, it enhances ion transport kinetics. Crucially, it regulates the decomposition sequence, allowing anions more prone to forming a high-quality interphase to be "sacrificed" during interfacial reaction, thereby kinetically protecting the solvent molecules.

In summary, the "solvent-reinforced" and "weakly solvating" strategies are not opposing but represent two distinct, effective pathways in advanced electrolyte engineering. The former is analogous to "consolidating internal affairs," enhancing intrinsic stability by strengthening internal bonds. The latter

resembles "skillful diplomacy," guiding the formation of an ideal interface by optimizing reaction sequence and kinetics. Their collective success reaffirms the core principle that the electrode/electrolyte interface ultimately dictates battery performance.

Supplementary note 3

The observed difference in the overcharge phenomenon between *in situ* differential electrochemical mass spectrometry (*in situ* DEMS) test and coin-cell cycling primarily stems from fundamental differences in the cell configuration and operational conditions of two tests. As illustrated in the provided schematic, *in situ* DEMS cell and standard coin cell differ significantly in structure and operating environment, leading to varied interfacial and kinetic behaviors.

(1) Key structural and operational differences

The observed discrepancy stems from fundamental distinctions between the two testing platforms, which establish vastly different interfacial and kinetic conditions for the same electrochemical reactions.

(a) Divergent design objectives and resulting structure

In situ DEMS cell: Engineered primarily for real-time gas analysis, its structure prioritizes gas transport over electrochemical interface quality. It employs a porous Al mesh current collector (*vs.* conventional foil) and features a grooved positive electrode column with a central vent to channel gases to the spectrometer. This design inherently compromises the intimacy and uniformity of electrode/electrolyte contact.

Coin cell: As a standard electrochemical testing platform, it is optimized for consistent electrical contact. It uses flat, dense current collectors and is sealed under high, uniform pressure, promoting a stable and homogeneous interface.

(b) Assembly process and interface quality

In situ DEMS cell: Uses a custom, reusable mold assembled manually. This process results in less uniform stack pressure distribution and greater variability, leading to a non-ideal, high-impedance interface prone to localized current hotspots.

Coin cell: Assembled using automated commercial equipment with precise, high-pressure crimping. This ensures reproducible and uniform interfacial contact, minimizing initial impedance and promoting even current distribution.

(c) Operational environment and reaction kinetics

In situ DEMS cell: Operates under a continuous argon purge, creating an open, dynamic system. Gaseous reaction products are immediately removed from the cell.

Coin cell: A hermetically sealed, static system. All gaseous and soluble reaction products accumulate within the confined cell volume, altering the local chemical environment.

These structural and operational differences collectively explain why the *in situ* DEMS test, while excellent for diagnosing failure mechanisms, presents a more accelerated and severe degradation profile compared to a standard coin cell test.

(2) Analysis of the discrepancy in overcharge behavior

The more pronounced overcharge observed in *in situ* DEMS test is attributed to the combined effects of inferior interface stability and an operational environment that kinetically promotes parasitic reactions.

(a) Accelerated interface degradation in *in situ* DEMS cell

Non-ideal interface contact: The grooved current collector and manual assembly of *in situ* DEMS cell result in less uniform pressure distribution at positive electrode interface compared to standard coin cells. This leads to inhomogeneous current distribution, localized high impedance, and exacerbated side reactions.

Consequence: A defective CEI forms more readily and is less effective. The increased and unstable interfacial impedance directly contributes to the severe overcharge phenomenon, as a greater fraction of

the charging time/energy is consumed by parasitic processes rather than useful Na^+ intercalation.

(b) Kinetic promotion of parasitic reactions in *in situ* DEMS cell

Product removal shifts reaction equilibrium: In *in situ* DEMS cell, the constant Ar flow immediately removes gaseous decomposition products (e.g., CO_2, C_2H_6). According to Le Chatelier's principle, this continuous product removal shifts the equilibrium of electrolyte decomposition reactions forward, promoting their continuous progression.

Contrast in coin cells: In a sealed coin cell, these gaseous products accumulate, increasing their partial pressure and thereby thermodynamically suppressing further decomposition. This natural self-inhibition moderates the rate of parasitic reactions and mitigates the overcharge effect over cycles.

In summary, the apparent discrepancy stems from the operational conditions of the *in situ* DEMS cell. Although excellent for operando gas analysis, its poor interfacial contact and product removal inadvertently accentuate the failure mechanisms of the unstable baseline electrolyte. The standard coin cell, with its more robust interface and sealed environment, provides a degree of inherent kinetic stabilization, allowing for more extended cycling despite the electrolyte's intrinsic instability. This comparison effectively highlights how cell design and testing conditions can significantly influence the observed degradation kinetics.

Supplementary note 4

The CEI acts as an electron-passivating layer between positive electrode and electrolyte. The bandgap E_g (CEI) of the CEI material fundamentally determines the electronic barrier properties, which in turn influence the electron tunneling probability. Electron tunneling through the CEI follows quantum mechanical principles, where the transmission probability decreases exponentially with both the height and the width of the potential barrier.

The bandgap directly governs the barrier height: a larger E_g corresponds to a higher energy barrier, which strongly suppresses electron tunneling, while a smaller E_g reduces the barrier and promotes tunneling. Additionally, the bandgap affects the availability of electronic states within the CEI that can participate in tunneling. Materials with a large bandgap provide fewer accessible states within the relevant energy range, further limiting tunneling probability. In contrast, materials with a smaller bandgap offer more accessible states, facilitating electron transfer via direct or trap-assisted tunneling mechanisms.

In battery operation, CEI components with an appropriately large bandgap can effectively block electron leakage from positive electrode to electrolyte, thereby mitigating parasitic reduction reactions and enhancing interfacial stability. This electronic passivation is crucial to suppress continuous electrolyte decomposition and CEI growth, ultimately improving cycling stability. For instance, in this study, boride/fluorides with bandgaps exceeding 6.2 eV are demonstrated to effectively inhibit electron tunneling above 4.0 V, thereby reducing current leakage and persistent interfacial side reactions.

Supplementary note 5

We conducted an in-depth study of the single-salt electrolyte (0.4M NaDFOB in EC/EMC, denoted as DE) and systematically compared its properties and performance characteristics with those of the DDSLE electrolyte (1M $NaPF_6$ + 0.4M NaDFOB in EC/EMC) and BE electrolyte (1M $NaPF_6$ in EC/EMC). The key findings are as follows:

(1) Oxidation stability

The DE electrolyte exhibits high intrinsic stability, with an anodic stability limit of 4.8 V, as demonstrated by linear sweep voltammetry (LSV) curves. However, the onset of oxidation occurs at a lower potential (around 3.8 V), which correlates with the progressive decomposition of the $DFOB^-$ anion. This indicates that NaDFOB alone provides sufficient intrinsic protection against oxidation but may not achieve the same level of stability as the mixed DDSLE system.

(2) Solvation configuration

Both the DE and DDSLE electrolytes exhibit similar anion coordination behaviors. Molecular dynamics simulations reveal that the $DFOB^-$ anions predominantly reside in the outer solvated Na^+ shell and do not participate in the inner-shell coordination. This consistent solvation behavior suggests that NaDFOB's solvation properties are comparable to those in the DDSLE system.

(3) Interphase structure

This is the core factor responsible for the performance divergence between the two electrolytes. Although $DFOB^-$ decomposition products (e.g., NaF, borates) are electrochemically stable, their interphase-forming processes and final morphologies differ fundamentally.

In the DE electrolyte, the positive electrode electrolyte interphase (CEI) and solid electrolyte interphase (SEI) are highly inhomogeneous and physically unstable. These interphases fail to provide effective passivation of the positive electrode or the Na negative electrode, leading to electrolyte decomposition and gas release. Additionally, the interphases exhibit poor mechanical stability, prone to fracture and dissolution during cycling, as evidenced by EQCM measurements.

In the DDSLE system, a sequential and synergistic decomposition occurs involving $DFOB^-$, PF_6^-, and solvents, resulting in the formation of a dense inorganic-rich inner layer and a flexible outer layer. This optimized interphase provides a balanced ionic conductivity and mechanical toughness, ultimately enabling the DDSLE system to achieve an ultra-long cycling life of over 16,500 cycles.

(4) Battery performance: contrast in reversibility and durability

The DE electrolyte supports a reversible Na (de)intercalation in NFS, with an initial Coulombic efficiency of 90.5%, confirming its fundamental electrochemical compatibility. However, its cell capacity decays rapidly after approximately 1500 cycles due to the inhomogeneous and unstable interphase to provide lasting protection.

In summary, while NaDFOB as the sole electrolyte salt offers a wide electrochemical window based on its high intrinsic oxidation stability, its interphase structure inherently lacks the homogeneity and mechanical stability required for long-term cycling performance. In contrast, the mixed-salt DDSLE system, on the other hand, leverages the unique properties of both $DFOB^-$ and PF_6^- to create an optimized interphase architecture. This strategy ensures superior intrinsic stability, interfacial protection, and overall battery performance.